Görtler Instability and Its Control via Surface Suction Over an Axisymmetric Cone at Mach 6

Fei Li,[*] Meelan Choudhari,[†] and Pedro Paredes[‡]
NASA Langley Research Center, Hampton, VA, 23681

Steven Schneider,[§] and Phillip Portoni,[**]
Purdue University, West Lafayette, IN 47907

The characteristics of Görtler instability over an axisymmetric cone with an aft concave section are studied via linear and nonlinear instability analysis and direct numerical simulations. Several options for the cone geometry have been investigated numerically, subject to a fixed forecone section and constraints on the maximum cone diameter, overall cone length, and minimum N-factor for the most amplified Görtler modes. Computations show that it is possible to design a cone with a peak N-factor of $N_{max} > 8$ at the target Reynolds number of 12.1×10^6 per meter, corresponding to the maximum quiet Reynolds number in the Boeing/AFOSR Mach-6 Quiet Tunnel at Purdue University. Direct numerical simulations show that an array of roughness elements corresponding to a peak roughness height of 0.1006 mm at the center can excite Görtler vortices that evolve into sufficiently strong streamwise streaks that may break down via high-frequency secondary instability. Thus, the selected axisymmetric configuration of interest should provide an acceptable baseline to investigate the feasibility of several aspects of laminar-flow control via boundary-layer suction. The apparatus that is being used for measurements in the Boeing/AFOSR Quiet Tunnel is described, along with some preliminary experimental results.

Nomenclature

A_u	=	local amplitude of Görtler vortex [m/s]
f	=	frequency of instability waves [kHz]
G	=	Görtler number, $(U_e\theta/\nu)(\theta/R)^{1/2}$
k	=	roughness height [mm]
k_{ref}	=	reference roughness height = 0.005 mm
M_∞	=	freestream Mach number
N	=	logarithmic amplification ratio
n	=	azimuthal wavenumber, i.e., number of waves across circumference
u	=	streamwise velocity [m/s]
U_e	=	boundary-layer edge velocity [m/s]
U_∞	=	freestream velocity [m/s]
P_∞	=	freestream pressure [Pa]
q_w	=	surface heat flux [W/m²]
R	=	streamwise surface radius of curvature [m]
Re	=	freestream unit Reynolds number [m⁻¹]
Re_θ	=	Reynolds number based on momentum thickness
t	=	time [sec]
T_w	=	wall temperature [K]

---

[*] Aerospace Technologist, Fei.Li@nasa.gov
[†] Aerospace Technologist, Meelan.M.Choudhari@nasa.gov, Associate Fellow, AIAA.
[‡] NASA NPP Fellow, pedro.paredesgonzalez@nasa.gov, Member, AIAA.
[§] Professor, steves@purdue.edu, Fellow, AIAA.
[**] Graduate Student, pportoni@purdue.edu, Student Member, AIAA.

American Institute of Aeronautics and Astronautics

T_∞	=	freestream temperature [K]
X	=	axial coordinate [m]
Y	=	wall-normal distance [m]
α	=	angle of attack [deg]
δ_H	=	boundary-layer thickness corresponding to 0.995 times total enthalpy in free stream [m]
κ	=	longitudinal surface curvature [m^{-1}]
μ	=	dynamic viscosity [Pa sec]
ν	=	kinematic viscosity [m^2/s]
ϕ	=	azimuthal coordinate with respect to windward meridian [deg]
θ	=	momentum thickness [m]
ρ	=	density [kg/m^3]

I. Introduction

Boundary layer transition from the laminar to a turbulent state is known to have a major impact on the design and performance of hypersonic flight vehicles. Additionally, boundary layer transition in nozzle wall boundary layers has a major impact on the freestream disturbance environment within the test section of high-speed wind tunnels. Acoustic radiation from turbulent boundary layers tends to dominate the overall disturbance field; therefore, transition control along the nozzle walls has been used as the basis to develop low disturbance (or the so-called quiet) wind tunnels that allow the ground facility measurements to mimic the transition characteristics during high-altitude flight.[1] For test section Mach numbers of six and above, the transition process within the approaching tunnel-wall boundary layers is dominated by the amplification of second (or Mack) mode instabilities[2] and/or centrifugal or Görtler vortex instabilities[3] along the concave, diverging section of the nozzle walls. The first mode instabilities may also play a role in transition, especially at Mach numbers of six or below. Furthermore, surface roughness is known to play a critical role, but the mechanism by which surface roughness affects transition is not fully understood.

The first generation of quiet hypersonic wind tunnels were built around the principle of removing the upstream boundary layer via surface suction near the nozzle throat, allowing a fresh boundary layer to form along the diverging section downstream. However, distributed suction over a larger acreage of the nozzle surface may become necessary to achieve an extended length of laminar region at higher Reynolds numbers (i.e., larger tunnel test sections) and/or larger Mach numbers. A preferred approach for implementing distributed suction employs microperforated skins; however, unavoidable nonuniformities in the discrete suction velocity distribution result in the generation of streamwise vorticity that may seed the Görtler vortex instabilities, offsetting the potentially stabilizing influence of the boundary layer suction. The present work is part of the initial phase of a computational and experimental effort aimed at investigating the technical risks associated with the use of distributed suction for the control of transition along the walls of a hypersonic nozzle. However, to facilitate controlled measurements in an affordable manner, attention is focused on the external boundary layer flow over a suitably designed cone model, instead of that along the walls of a wind tunnel nozzle. The initial computational work is focused on the design of a wind tunnel model that can support a strong linear amplification of Görtler vortices while satisfying the geometric constraint associated with the wind tunnel. An additional goal is to examine the various different phases of Görtler vortex evolution in the absence of any suction, including receptivity, linear and nonlinear evolution, and high-frequency secondary instability of stationary Görtler vortices. On the other hand, the initial phase of the experimental measurements is focused on risk reduction related to the effects of distributed suction through a perforated surface.

Hall[4–6] showed that for relatively modest surface curvature with a Görtler number of G = O(1), the amplification of Görtler vortex instabilities is governed by a parabolic set of equations and that the streamwise length scale of amplitude growth is comparable to the body length scale over which the basic state evolves. Effects of compressibility on the Görtler instability have been examined in Refs. [7–20]. Specifically, Fu et al.[10–12] first used high Reynolds number asymptotic methods to study the Görtler instability in hypersonic boundary layers. Numerical studies of the various aspects of the same problem were performed by Whang et al.[15–18] Secondary instability characteristics of finite amplitude Görtler vortices in hypersonic flows were studied by Li et al.[19] in both internal nozzle wall boundary

layers and external boundary layer over a flared cone and subsequently by Ren and Fu[20] in the context of model boundary layer flows.

An outline of the paper is as follows. Section II is devoted to the compution of mean flow characteristics and stability properties of several candidate geometries of an axisymmetric cone model for wind tunnel measurements in the Boeing/AFOSR Mach-6 Quiet Tunnel (BAMQT) at Purdue University. Computations are performed for a total of 13 such configurations to identify a suitable model design for the experimental investigation that will eventually focus on the effects of suction on instability development in the boundary layer flow over one or more slected models. The focus of these initial computations is on the zero suction case, to help understand the instability characteristics of the baseline configuration. Section III presents a summary of direct numerical simulations pertaining to the generation of Görtler vortex instabilities, their linear and nonlinear amplification, and secondary instability. Section IV outlines the overall concept for the experimental campaign, model hardware design including the implementation of surface suction and the surface mounted instrumentation, and preliminary measurements in the BAMQT. Summary and concluding remarks including plans for the follow-on work are presented in Section V.

II. Design and Analysis of an Axisymmetric Cone

A. Flow Conditions and Analysis Codes

The flow conditions of interest correspond to the nominal maximum quiet flow Reynolds number in the Boeing/AFOSR Mach-6 Quiet Tunnel at Purdue University, namely, a freestream Mach number of $M_\infty = 6$, unit Reynolds number $Re = 12.13 \times 10^6$ per meter, freestream static pressure of 702.62 Pa, and a freestream temperature corresponding to $T_\infty = 51.92$ K. The temperature of the model surface, T_w, is equal to 300 K.

The unperturbed boundary-layer flow over the cone is computed using the VULCAN (Viscous Upwind aLgorithm for Complex flow ANalysis) software.[21] The working fluid is assumed to be perfect gas (air) and the usual constitutive relations for a Newtonian fluid are used: the viscous stress tensor is linearly related to the rate-of-strain tensor, and the heat flux vector is linearly related to the temperature gradient through Fourier's law. The coefficient of viscosity is computed from Sutherlands's law, and the coefficient of thermal conductivity is computed by assuming a constant Prandtl number Pr = 0.71. The VULCAN code solves the unsteady, conservation equations appropriate for laminar or turbulent flow of calorically or thermally perfect gases with a spatially second-order accurate cell-centered finite-volume scheme. In the present computations, the inviscid fluxes were constructed using the MUSCL κ=0 scheme, the van Albada gradient limiter[22] and the Low Dissipation Flux Split Scheme (LDFSS) of Edwards.[23,24] The cell face gradients required to construct the viscous fluxes were obtained using an auxiliary control volume approach that results in a compact viscous stencil that produces a second-order accurate approximation of the full Navier-Stokes viscous fluxes. In previous work, similar computations of the mean flow over an elliptic cone configuration were cross-verified against the solutions obtained with the LAURA code[25] for various grid sizes.[26]

The generation of stationary Görtler vortex instabilities and their subsequent evolution in the boundary-layer flow is computed by using a high-order DNS solver used by Li et al.[27] A detailed description of the governing equations and their numerical solution is given by Wu et al.[28] The inviscid fluxes from the governing equations are computed using a seventh-order weighted essentially nonoscillatory finite-difference WENO scheme introduced by Jiang and Shu;[29] the present scheme also allows the use of limiters that have been optimized to reduce the numerical dissipation. Both an absolute limiter on the WENO smoothness measurement and a relative limiter on the total variation are employed simultaneously during the simulation. The viscous fluxes are discretized using a fourth-order central difference scheme and time integration is performed using a third-order low-storage Runge-Kutta scheme.[30] The numerical code has been previously applied to simulation of turbulence in hypersonic boundary layers[31] as well as laminar-turbulent transition due to crossflow instability in swept wing boundary layers.[32,33] The lessons learned from these simulations were applied to develop the computational grid for stationary crossflow evolution in the present work.

In the DNS computations, the stationary Görtler vortices are excited via an array of axially localized roughness elements centered at selected axial stations. The roughness array consists of pairs of smooth shaped vortex generators with an inclination of 8 degrees with respect to the inviscid flow near the boundary layer edge, an axial length of 1.1 mm, and a specified combination of azimuthal wavenumber $n = 100$ (where n denotes the number of vortex wavelengths across the full circumference of the circular cone) and peak roughness height k.

3

American Institute of Aeronautics and Astronautics

B. Cone Geometry

A schematic of the axisymmetric cone configuration is shown in Figure 1. The overall configuration is partitioned into two separate sections along the axial length of the model. The upstream section allows the incorporation of a perforated-skin segment for boundary layer suction and, for simplicity, it is constrained to a 7-degree half-angle cone with a nose radius of 0.1 mm and an axial length of at least 0.25 meters. The downstream section includes a region of concave wall (chosen to have a fixed radius of curvature, R_b, to simplify the shape specification) that would sustain sufficiently strong amplification of Görtler vortex instability. To simplify the geometry specification, the geometry of the downstream section is parameterized with a small number of variables as indicated in Fig. 1. To avoid any difficulties with tunnel startup, the maximum diameter of the aft section is constrained to 0.1143 meters (4.5 inches). To allow a smooth mating with the forecone section, the upstream end of the aft section corresponds to an extension of the forecone section. Transition from the forecone to the constant radius concave segment is achieved via a short, convex portion of radius R_t.
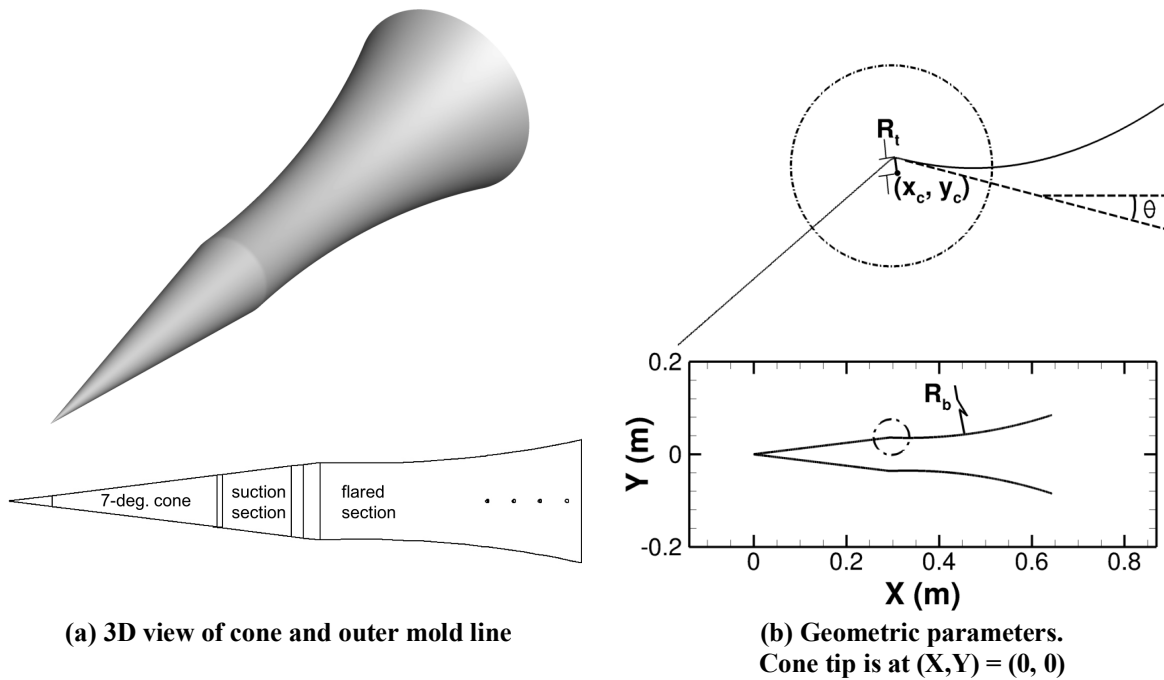

(a) 3D view of cone and outer mold line

(b) Geometric parameters.
Cone tip is at (X,Y) = (0, 0)

Figure 1.   Schematic of axisymmetric cone with a concave aft section.

The length of the straight-cone, the radius of the small joining arc, the radius of the concave and the initial slope of the aft-body can be varied respectively to construct different geometric configurations and thus enable a parametric study of the resulting flow field. As described in Table I, a total of 13 configurations have been examined to date in order to provide insights into the effects of these parameters on the basic state and the instability amplification characteristics. As mentioned earlier a roughness array is used in the computations to generate Görtler vortices, a pair of roughness elements symmetrically placed within a single azimuthal wavelength of 3.6 degrees is shown in Fig. 2. This pattern is repeated around the circumference of the cone. The array shown is centered at X = 0.260 m, over the junction of the forebody and the aft-body.
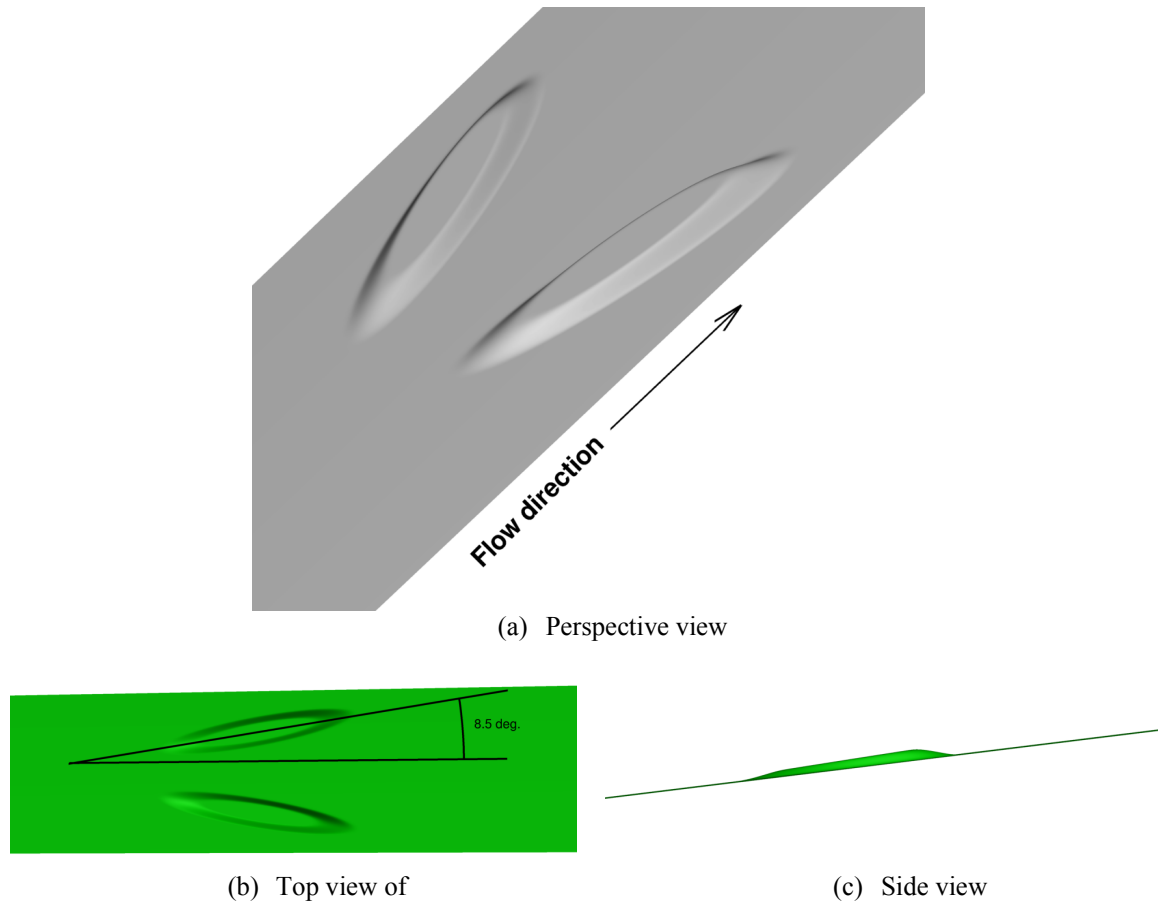
American Institute of Aeronautics and Astronautics

(a) Perspective view

(b) Top view of

(c) Side view

Figure 2. Roughness elements symmetrically placed within an azimuthal wavelength of 3.6 degrees.

Table I Cone geometries investigated in this paper. The highlighted rows are cases not used for stability analysis. Case 9 design is used in the experiment.

Case	R_t (m)	R_b (m)	Cone half angle (deg)	Smooth Curvature	X_c (m)	Grid size	θ (deg)	Cone Length (m)
1	0.03	3.0	7	N	0.44436	2241×513	6	0.800
2	0.03	3.0	7	N	0.44436	2241×513	6	0.800
3	0.15	0.7	7	N	0.31828	2177×513	12	0.760
4	0.15	0.5	7	N	0.45898	2241×513	14	0.760
5	0.60	1.0	4	N	0.29185	2177×513	2	0.624
6	0.60	1.0	7	N	0.32312	2177×513	2	0.591
7	0.40	1.0	7	N	0.33775	2177×513	2	0.583
8	0.03	1.0	7	N	0.29266	2241×513	2	0.537
9	0.03	1.0	7	Y	0.29266	2241×513	2	0.541
10	0.03	1.0	7	N	0.29266	2241×513	3	0.558
11	0.03	1.0	7	N	0.29266	2241×513	4	0.582
12	0.03	1.0	7	Y	0.29266	2177×513	-7	0.408
13	0.60	1.0	7	N	0.51382	2241×513	-2	0.471

American Institute of Aeronautics and Astronautics

All configurations from Table I, with the exception of configurations 9 and 12, include a discontinuity in curvature at both upstream and downstream ends of the transition section. To assess the effect of those discontinuities on instability amplification, the transition section for configurations 9 and 12 was designed to vary the surface curvature in a smooth manner from a value of zero at the upstream end (where the transition section merges with the forecone section) to a value of $-1/R_b$ at the beginning of the concave aft-body. The length of the hump is varied to achieve a continuous slope distribution across the transition section. This procedure leads to a small increase in the cone length (< 5 mm) relative to the corresponding shapes with a circular arc transition section with discontinuous curvature distribution. Three representative outer mold lines of the various configurations are depicted in Fig. 3. Cases 3 and 4 were designed to provide significantly stronger curvature ($R_b < 1.0$ m) than all of the remaining cases ($R_b \geq 1.0$ m). To yield a reasonable length of concave portion without exceeding the permissible cone radius, these two configurations involve large initial angles of the concave surface ($\theta = 12$ and 14 degrees, respectively). The steeper inclination leads to flow separation near the beginning of the concave section. On the other hand, case 11 exhibits a long separation bubble close to the concave surface. The above three cases (highlighted in orange in Table I) with flow separation were excluded from further investigation involving boundary layer stability analysis, and hence, have been flagged with orange highlighting in Table I. Similarly, by virtue of the longer straight cone section, case 13 violates the constraint on the maximum cone radius even before the beginning of the concave section, and hence, has been flagged with red maroon highlighting.
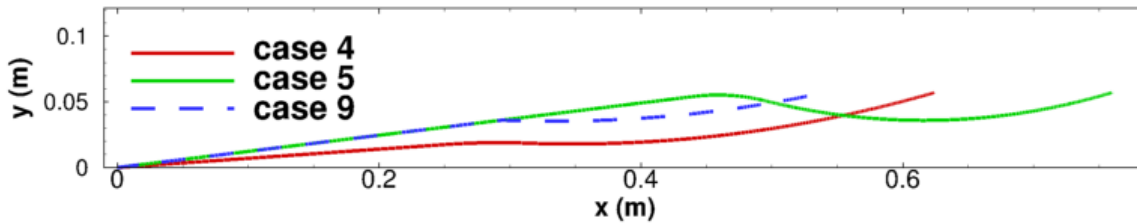

Figure 3. Outer mold lines of various cone configurations listed in Table I.

C. Mean Flow Computation

Mean flow computations were carried out for all configurations from Table I, and their instability characteristics of the unhighlighted cases were investigated. In general, a larger cone length implies a longer section of concave surface curvature, and hence, a potentially higher amplification factor for the Görtler vortices. When the initial slope of the concave section is negative, the cone radius initially decreases with x before increasing again. This allows a longer aft section subject to the overall constraint on the maximum cone radius. However, if the initial negative slope is too large, then the flow is likely to separate, which must be avoided. Computations showed that an initial slope of -2 degrees provided a long enough aft section without inducing flow separation. Figure 4 shows the Mach contours for Case 9 from Table I, which were computed using the VULCAN code. An expansion fan is observed to originate in the vicinity of the hump that joins the fore- and aftbodies. Farther downstream, the flow field undergoes a compression due to the concave surface curvature, eventually resulting in the formation of a shock wave beyond $x = 0.55$ m. Therefore, a wind-tunnel model based on this design should not exceed 0.55 meters in length.
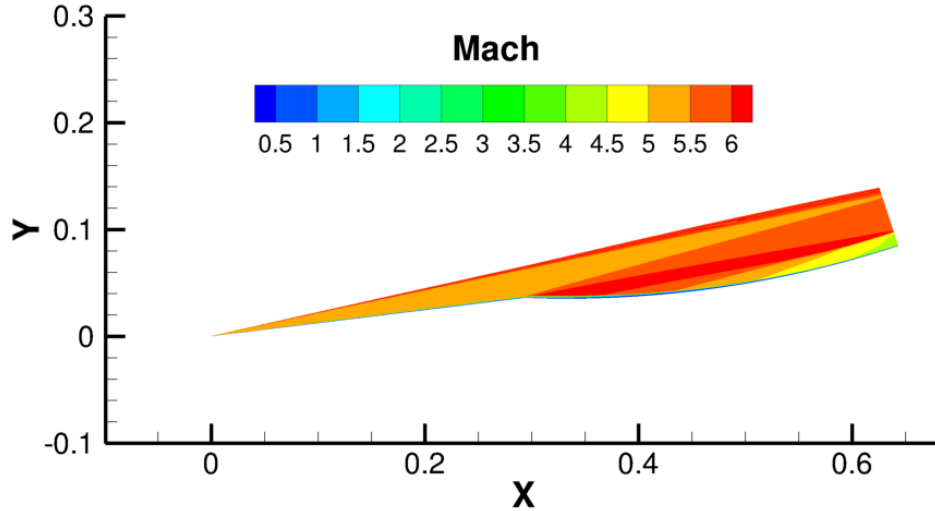
6

American Institute of Aeronautics and Astronautics

Figure 4.   Mach number contours for Case 9 in Table I.

To demonstrate the insensitivity of the computed mean flow to grid resolution, the VULCAN solution is compared with the flow solutions computed on two different grids by using the DNS code. To reduce the computational cost of the DNS solution, the inflow boundary for the DNS computation is set a $X = 0.1$ m and the top boundary is set to just below the shock wave. The VULCAN solution at $X = 0.1$ m and below the shock is imposed as the inflow and top boundary condition for DNS, while a sponge region is used at the outflow boundary. The larger DNS grid in Fig. 5 uses the same streamwise grid as the VULCAN computation, but the wall-normal grid includes every other point from the VULCAN grid. As shown by the surface pressure distributions (Fig. 5(a)) and surface heat flux distributions (Fig. 5(b)), respectively, both inviscid and viscous metrics of the solution are seen to compare very well between the various computations. As seen in Fig. 5(a), the flow undergoes a rapid expansion over the narrow hump joining the straight and the concave sections. This expansion is reflected via a sharp drop in the wall pressure just upstream of $X = 0.3$ m, which is also accompanied by similarly rapid decrease in the surface heat flux. Downstream of the transition section, the pressure recovers gradually and the wall heat flux also increases correspondingly.
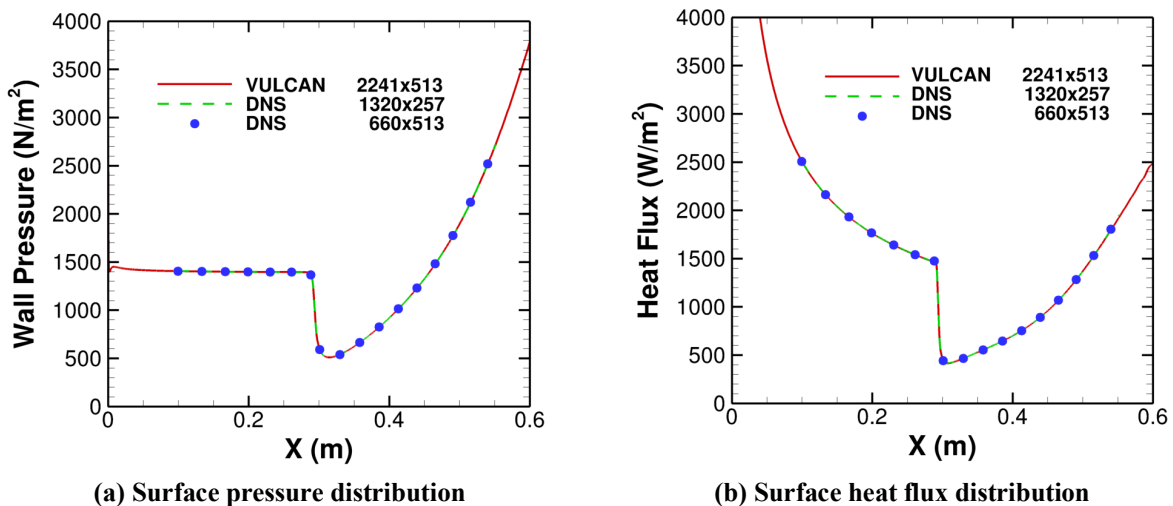

(a) Surface pressure distribution

(b) Surface heat flux distribution

Figure 5. Comparisons of surface pressure and heat flux distributions on different grids and/or via different numerical schemes.

7

American Institute of Aeronautics and Astronautics

D. Stability Characteristics

As shown by Hall[4,5] the Görtler instabilities are governed by a parabolic system of equations for O(1) values of the Görtler number, *G*. In this case, the length scale of Görtler vortex amplification is comparable to the streamwise length scale of the mean boundary layer. A local eigenvalue analysis of the Görtler problem is not justified and the amplification characteristics based on the parabolic system depend on the initial disturbance profiles, which must be chosen either in an ad hoc manner or by solving the receptivity problem for a given forcing field. The ad hoc selection of inflow profiles leads to an ambiguity in characterizing and/or comparing the growth potential of Görtler vortices between different flow configurations. Fortunately, for the configurations of interest in this paper, the peak Görtler number is substantially larger than unity. Thus, the non-parallel effects are secondary, and to the leading order, N-factors for the disturbance wavenumbers of interest can be predicted via quasi-parallel stability theory or by integrating the parabolic system of governing equations by starting at the neutral station with a mode shape based on local eigenvalue analysis.

Linear N-factor computations for stationary modes of Görtler instability are carried out for various azimuthal wavenumbers, *n*, and the results are shown in Figure 6 along with the surface geometry of the cone (Fig. 6 (a)). The N-factor results indicate that the most amplified Görtler mode has an azimuthal wavenumber of approximately 130, which achieves an N-factor of nearly 8 near the end of the cone. The amplification of the Görtler instability extends across a broad range of wavenumbers and vortices within the range of *n* = 100–220 have maximum N-factors of 7 or larger. Although not shown, the peak N-factors associated with Görtler vortex amplification in cases 6 through 8 and case 10 are close to the peak N factor in case 9. The corresponding azimuthal wavenumber is also comparable to that in case 9, with a value of between *n* = 125 to *n* = 145. The Görtler instability in cases 1, 2, and 12 is much weaker, with a peak N-factor that is less than 5.

An alternative to the above procedure consists of maximizing the growth of a specified disturbance norm across a specified streamwise interval. Optimal growth computations (or, equivalently, input-output analysis) of this type for an incompressible boundary layer were presented by Cossu et al.[35] Analogous results for the flow configuration 9 from Table I are presented in Fig. 6(b), wherein we compare the N-factor evolution based on input-output analysis and the PSE calculations initialized with local eigenfunction near the neutral station. Because the optimal growth analysis is designed to maximize the growth in the selected energy norm, it yields higher N-factor values than those based on conventional PSE marching. The difference in peak N-factors is mainly attributed to conventional transient growth mechanism within the non-concave portion fo the model. It should be noted, however, that such growth requires a special type of inflow disturbances that may not be easily realizable in a natural disturbance environment. Thus, the results predicted by the optimal growth analysis should be viewed as providing an upper bound on the magnitude of disturbance growth up to a specified streamwise station.
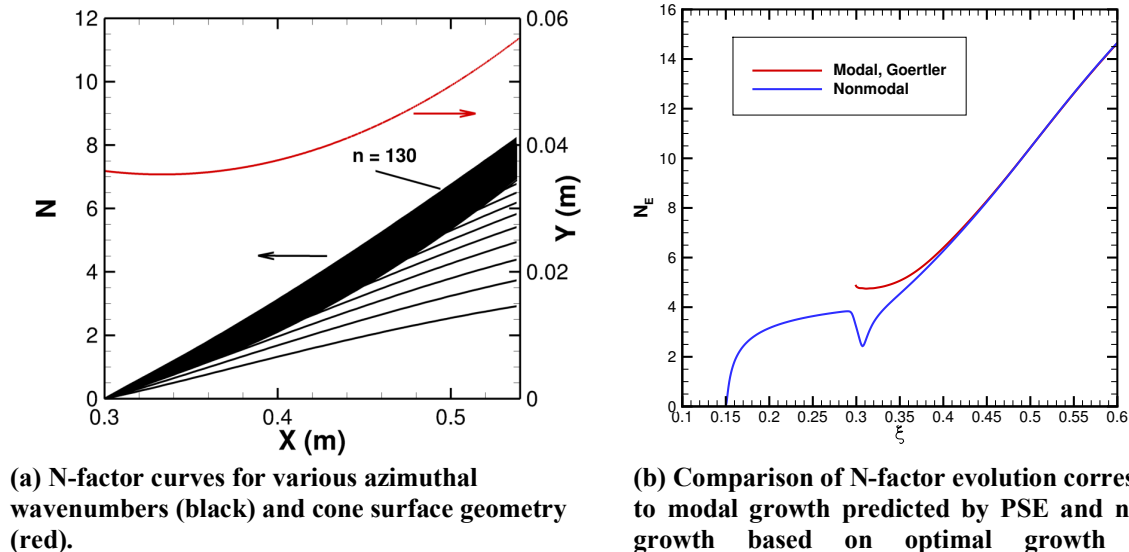

(a) N-factor curves for various azimuthal wavenumbers (black) and cone surface geometry (red).

(b) Comparison of N-factor evolution corresponding to modal growth predicted by PSE and nonmodal growth based on optimal growth analysis (disturbance wavenumber corresponds to *n* = 100)

Figure 6. Görtler N-factors for various azimuthal wavenumbers (Configuration 9 from Table I).

American Institute of Aeronautics and Astronautics

Figure 7 shows the streamwise variation in Görtler number for configuration 9 from Table I. The maximum value of the Görtler number at the Reynolds number of interest is approximately 20. Beckwith and Holley[34] had made measurements inside two different Mach 5 nozzles and found that the onset of transition in the concave section of the nozzle was associated with a local Görtler number of 5 to 6. For configuration 9, the above value is exceeded very close to the start of the concave section. On the other hand, N-factor correlations by Beckwith and Holley[34] had revealed a wide spread in the transition N-factor from 4 to 15. Since the maximum N-factor for configuration 9 falls within the above range, transition due to Görtler vortices is likely to occur at the baseline Reynolds number; however, whether or not transition onset will indeed occur will depend on the disturbance environment, and in particular, on the surface finish characteristics of the cone model.
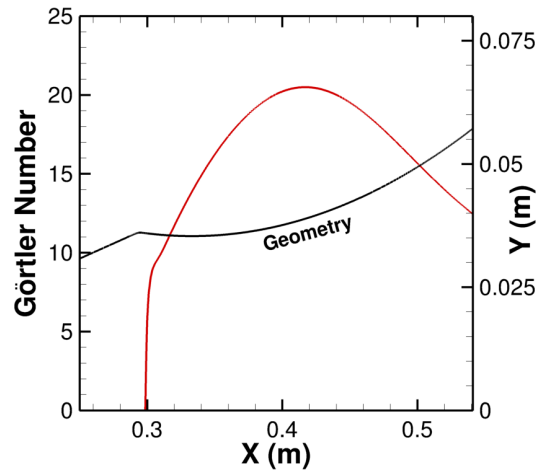
Figure 7.   Axial distribution of Görtler number G for configuration 9 from Table I.

Amplification characteristics of Mack mode instabilities for configuration 9 are shown in Fig. 8.   Mack-mode transition in benign disturbance environments such as flight or hypersonic quiet tunnels requires N-factors of 14 or even larger. Thus, the results of Fig. 8 indicate that Mack mode amplification is not likely to be a dominant cause for transition on configuration 9. The relatively sharp transition between straight and concave sections of the cone leads to a separation between Mack mode amplification over those two regions. The peak N factor for Mack modes over the straight cone section ($X < 0.30$ m) is approximately equal to 4, indicating that the flow is unlikely to transition over the straight segment, regardless of whether the wind tunnel is operated in quiet or noise mode.
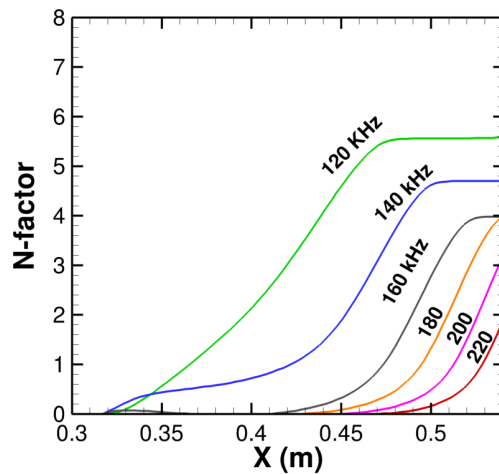

Figure 8.   Mack mode N-factors for selected frequencies (Configuration 9 from Table I)

9

Although not shown, the Mack mode amplification in cases 5 through 10 is rather similar, with a peak N-factor value that is very close to that shown in Fig. 8 for case 9.

III. Excitation of Most Amplified Görtler Modes and Their Downstream Evolution

If natural transition due to Görtler vortex instability does not occur on configuration 9, then artificial excitation of Görtler vortices may be necessary to induce transition over the cone model.

A. Excitation of a Dominant Görtler Mode (n= 100)

To examine the receptivity process in a DNS setting, an azimuthally periodic array of roughness elements is introduced on the cone surface for the purpose of generating streamwise vortices that seed the Görtler vortex instability in the downstream region. Within each azimuthal wavelength of the targeted vortex wavenumber ($n = 100$), a pair of vortex generators is placed symmetrically at an inclination of 8.5 degrees with respect to the cone generatrix. Each vortex generator has a ramp shape in the streamwise direction, with a linearly increasing height over a majority of its length. The x locations of the roughness elements are varied to study the effectiveness of streamwise placement. The middle of the transition section corresponds to $X = 0.2937$ m. DNS results shown in Fig. 9(a) indicate that placing the roughness elements upstream of the hump is more effective than roughness elements within the transition section or over the concave section. As shown in Figure 9(a), when roughness location is at or just downstream of $X = 0.2937$ m, the resulting perturbations reach comparable amplitudes downstream, whereas the upstream placed roughness pair at $X = 0.280$ m increases the perturbation amplitude by an order of magnitude. Pushing the roughness pair farther upstream to $X = 0.260$ m nearly doubles the amplitude near the outflow of the computational domain. Moving the roughness location even farther upstream to $X = 0.230$ m continues the trend, but the incremental increase in amplitude becomes very small.

Figure 9(b) shows the effect of roughness height for a fixed roughness array location of $X = 0.26$ m. The amplitude of the vortex perturbation is found to increase at a faster than quadratic rate as the peak roughness height is increased. A comparison of N-factor predictions based on DNS for the smallest-height roughness array with $k/k_{ref} = 0.2$ and linear PSE calculations is shown in Fig. 10(a), whereas velocity contours at $X = 0.492$ m for the larger height roughness elements with $k/k_{ref} = 1$ and $X_0 = 0.29365$ m are displayed in Fig. 10(b). The differences between the PSE and the DNS are limited to the initial region of Görtler vortex amplification and we attribute these differences to the inflow transient in the PSE prediction because of inflow disturbance profile.   One may also observe the similarity between the N-factor evolution based on the DNS solution and the optimal evolution for $X > 0.3$ m in Fig. 6(b). The shape of the velocity contours resulting from the nonlinear evolution of the Görtler vortex (Fig. 10(b)) indicates that the Görtler vortices excited by the larger height roughness array can achieve high enough amplitudes to induce a strong upwelling of the velocity contours. The resulting mean-flow streaks are likely to sustain rapidly amplifying high-frequency instabilities that lead to the onset of laminar-turbulent transition within the boundary layer.
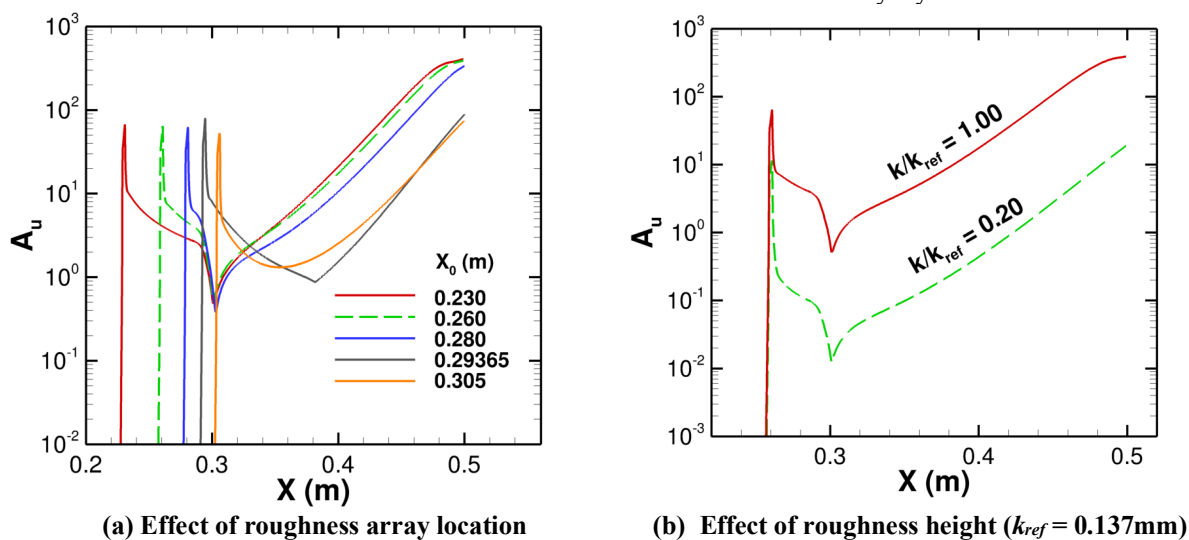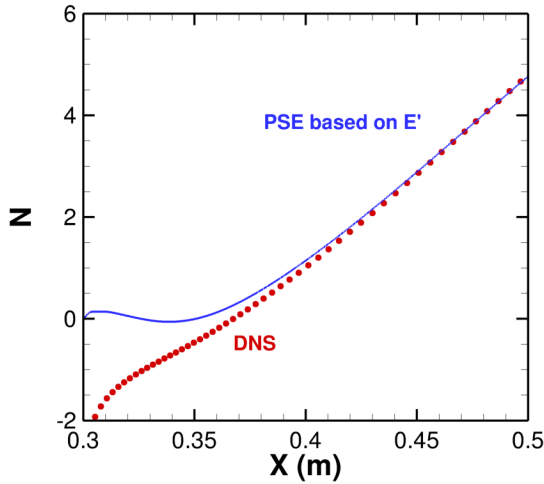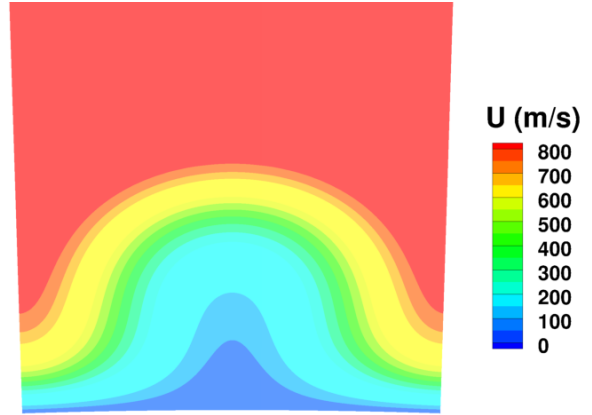

(a) Effect of roughness array location (b) Effect of roughness height ($k_{ref} = 0.137$mm)

Figure 9. Streamwise evolution of Görtler vortex excited by a roughness array with $n = 100$.

American Institute of Aeronautics and Astronautics

(a) Comparison of N-factor evolution
based on DNS and PSE

(b) Streamwise velocity contours across a single
wavelength of the Görtler vortex ($X = 0.492$ m)

Figure 10. DNS of Görtler vortex excited by a roughness array with $n = 100$, $k/k_{ref} = 1$, $X_0 = 0.28365$ m

B. Secondary Instability Characteristics

Nonlinear Görtler vortices such as those presented in Figure 10(b) lead to inflectional profiles in both wall-normal and spanwise directions. As such, they are susceptible to various families of high frequency secondary instability, which have previously been studied in the context of incompressible flows using simplified, inviscid secondary instability models.[36,37] Li et al.[19] analyzed the secondary instability of Görtler vortices in high speed boundary layers by using a fully viscous, spatial stability model that has also been used to compute secondary instability of crossflow vortices.[38]
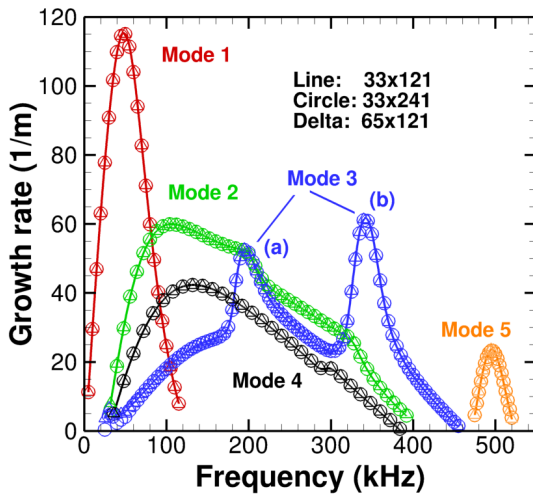
(a) Growth rate spectra for secondary instability
modes at $X = 0.498$ m
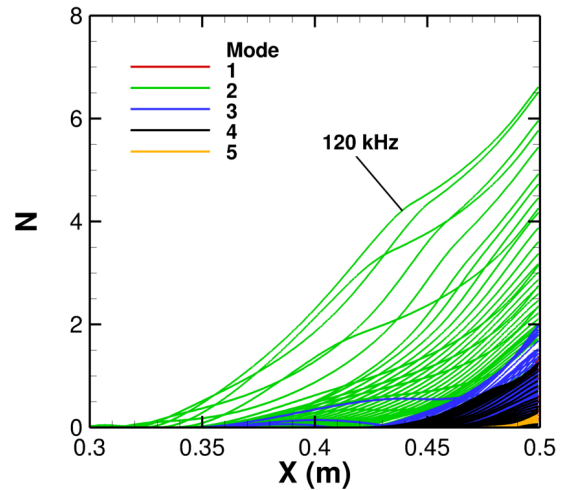
(b) N-factor evolution for fixed frequency
disturbances belonging to modes 1
through 5 from part (a)

Figure 11. Secondary instability characteristics of Görtler vortices for the case shown in Figure 10.

American Institute of Aeronautics and Astronautics

For the Görtler vortices computed via DNS for the $k/k_{ref} = 1$ and $X_0 = 0.29365$ m case, as many as five families of unstable secondary instabilities have been identified at $X = 0.498$ m (Fig. 11(a)). These are designated modes 1 through 5, respectively, and the N-factor evolution for various fixed-frequency disturbances belonging to each of those five modes is plotted in Fig. 11(b). The N-factor values are obtained via spatial integration of local growth rates obtained by local, quasiparallel secondary instability analysis. Even though the (local) peak growth rates of modes 1 and 3 are higher than the (local) peak growth rate of mode 2 according to Fig. 11(a), it is the mode-2 disturbances that exhibit the highest amplification factors as seen from Fig. 11(b). The mode 2 disturbance with a frequency of 120 kHz achieves the highest N-factor of slightly above 6.5 at the end of the DNS domain ($X = 0.5$ m). Extrapolating the N-factor envelope to the end of the cone, one obtains a peak N factor of nearly 8, which could well lead to transition via the nonlinear evolution of the secondary instabilities. Nonlinear Görtler vortex breakdown at hypersonic Mach numbers was investigated via DNS in the previous work of Li et al.,[38] in the context of Görtler instability in the nozzle wall boundary layer of the BAMQT facility at Purdue University.

The mode shapes for all five secondary instability modes at $X = 0.498$ m are shown in Figure 12, which would correspond to the root-mean-square values mapped out by a probe traversing across the vortex cross section at the specified streamwise station. The most amplified mode (mode 2) is symmetric with respect to the vertical symmetry line between a pair of counter-rotating Görtler vortices, so that the associated fluctuations in the streamwise and wall-normal velocity fluctuations and the temperature fluctuation on both sides of the symmetry line are in phase. Modes 3 and 5 are also symmetric modes, whereas modes 1 and 4 are anti-symmetric modes. Modes 3b and 5 correspond to the distorted form of higher Mack modes, whereas modes 1, 3a, and 4 appear to denote shear layer instabilities associated with the regions of high means shear near the boundary of the Görtler vortex. The latter modes do not become unstable in the absence of the Görtler vortices. Li et al.,[38] had observed that the secondary instability of Görtler vortices in hypersonic boundary layers is, in general, dominated by large temperature fluctuations, in contrast to the low Mach number case where velocity fluctuations dominate.[37]

A comparison of the growth rate spectra (not shown in this paper) with and without the fine amplitude Görtler vortices indicates that the dominant mode of secondary instability (mode 2) originates from the unstable Mack mode of the unperturbed boundary layer. Thus, the mode 2 eigenfunction in Fig. 12 indicates how the Mack mode perturbations get distorted via interaction with the stationary Görtler vortices. A similar connection has also been found between the secondary instability of stationary crossflow vortices and Mack modes in the unperturbed mean boundary layer over a yawed cone.[39–41] We also note that for the moderate amplitude vortex considered herein, the peak growth rate (as well as the associated frequency) of the most amplified mode-2 disturbance is close to the dominant Mack mode instability in the unperturbed boundary layer. The main effects of the finite amplitude Görtler vortices include a broadening of the frequency band of unstable disturbances (see Fig. 11(a)), strong distortion of the mode shape, and a modest change in the growth rate. In follow-on work, it will be interesting to examine the effects of the nonparallel evolution of the secondary instability modes, analogous to the work by Li et al.[40] for secondary instabilities of crossflow vortices.

Although not shown, we have also investigated secondary instability modes with longer azimuthal wavelengths that correspond to the first subharmonic of the Görtler vortices. Similar to the findings by Paredes et al.[42] for optimal growth streaks over circular cones without concave curvature, the subharmonic mode can have higher peak growth rates than those of the fundamental modes. However, because the subharmoic modes originate as shear layer instabilities, they become unstable only after the Görtler vortices have become sufficiently strong. Thus, they begin to amplify significantly downstream of the fundamental wavelength mode that originates from Mack mode instabilities, and hence, begins to amplify even when the Görtler vortex is rather weak. Consequently, the highest N-factors within the length of the cone are still achieved by the latter fundamental mode.
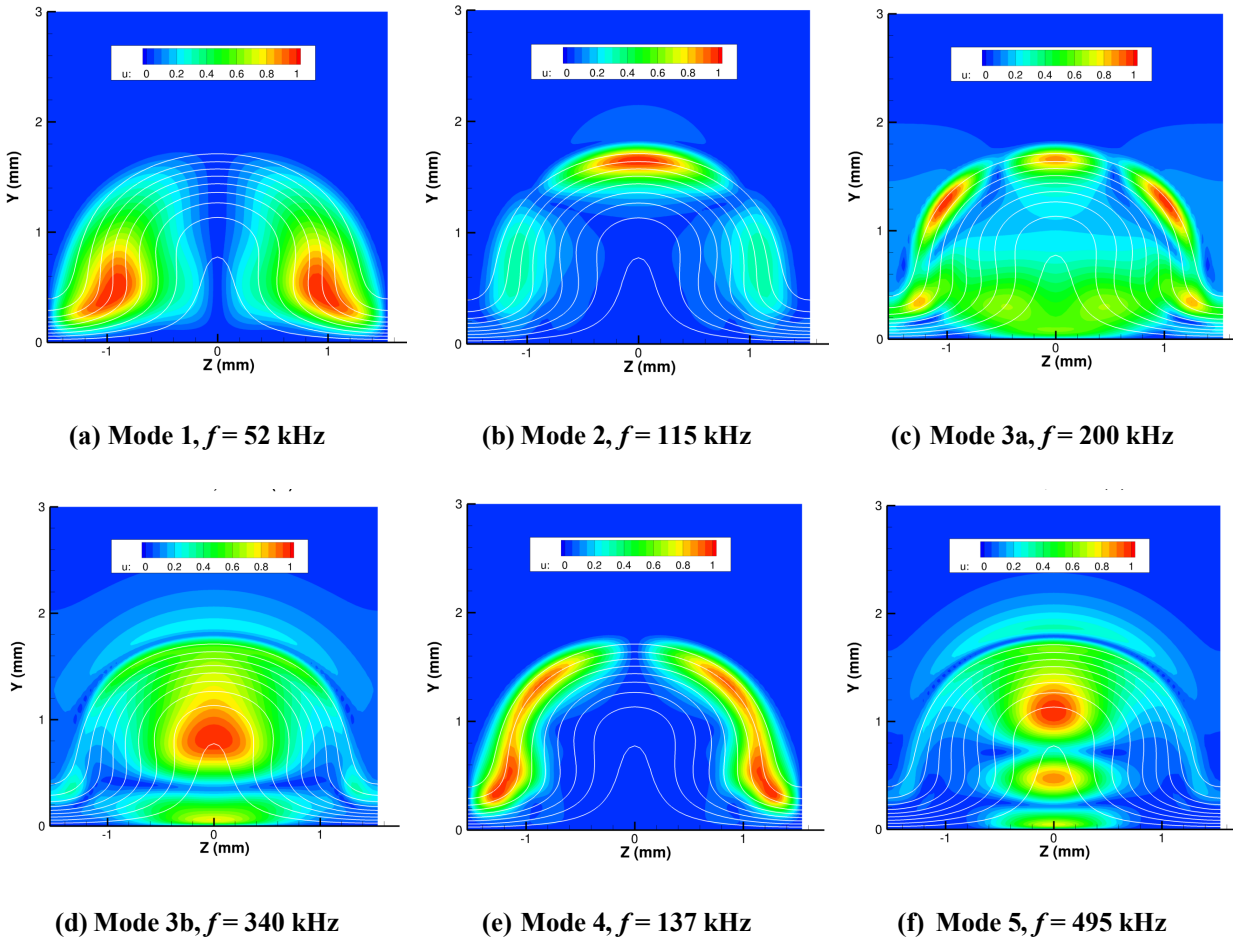
American Institute of Aeronautics and Astronautics

(a) Mode 1, f = 52 kHz   **(b) Mode 2, f = 115 kHz**   **(c) Mode 3a, f = 200 kHz**

(d) Mode 3b, f = 340 kHz   **(e) Mode 4, f = 137 kHz**   **(f) Mode 5, f = 495 kHz**

Figure 12. Representative eigenfunctions for streamwise velocity perturbations associated with five dominant modes of secondary instability at X = 0.498 m. The white lines represent the streamwise velocity contours associated with the basic state. The eigenfunctions are normalized so that peak velocity fluctuation is equal to unity.

IV. Experiments

A brief summary of the accompanying experimental effort at Purdue University is provided in this section.

A. *Brief Summary of Overall Concept for the Experiments*

Although the use of suction for maintaining laminar flow over supersonic wind-tunnel nozzles was investigated by Klebanoff et al., Beckwith et al. and Pfenninger et al. during the 1960's and 1970's (see, e.g., Ref. 1), it was not successful, apparently because of the nonuniformity of the suction and the roughness of the sintered-metal suction surfaces that were used at the time. The present experiments were undertaken to determine if newer technology for manufacturing microporous surfaces might make quiet nozzles with suction feasible.

Suction through a microporous wall is inevitably nonuniform, since it occurs through many small orifices. The resulting nonuniformities introduce streamwise vorticity, which might amplify via the Görtler instability. They may also be unsteady, generating perturbations that may radiate into the flow above the suction surface. Furthermore, the beginning and end of the suction will introduce compression and expansion waves into the flow above the surface,

13

American Institute of Aeronautics and Astronautics

disturbing the flow. In addition, the suction surface must withstand the startup and shutdown loads associated with the wind-tunnel operation, and these loads are quite large in a quiet Ludwieg tube with a downstream valve. To evaluate these four risks in an affordable way, small suction sections are being fabricated by Calspan Systems Corp. of Newport News, Virginia and CAV Advanced Technologies Ltd. of the United Kingdom, for experiments in the Mach-6 quiet tunnel at Purdue, using a model designed by NASA Langley and Purdue. Although another critical issue is whether reasonable levels of suction can damp or remove the Görtler instabilities on a concave wall, that Görtler-damping effect is not tested in this first phase of the work, since it would require a much larger and more expensive suction section.

B. Design and Fabrication of the Model and Suction Sections

The suction section, sketched in Fig. 13, was designed to attach to the end of a simple 7-deg. sharp-cone nose section. Since the cone has a developable surface that can be unrolled flat, fabrication of the initial suction surfaces is less expensive. The maximum stagnation pressure for quiet flow in the Mach-6 tunnel has been about 170 psia, leading to a boundary-layer thickness at the suction section that is computed to be about 1 mm, so that it is possible for feasible suction holes to be much smaller than the boundary-layer thickness.

The suction region is about 1 inch long and 2-1/2 inches in diameter. The red skin shown in Fig. 13 is a microperforated titanium sheet fabricated by CAV-AT of the United Kingdom. Several different interchangeable suction sections are being fabricated using different perforation patterns for the skin. The red skin is electron-beam welded to the titanium suction body, shown in blue in Fig. 13.
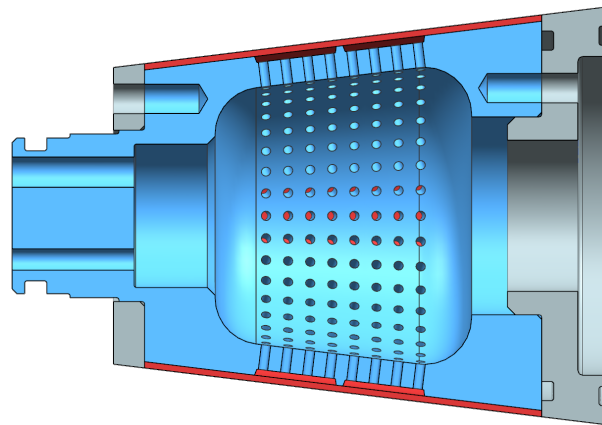

Figure 13.   Schematic of suction section for cone-clare model.

The first suction section was completed in July 2017, as shown in Fig. 14. The titanium skin contains roughly 200,000 holes, each about 50 microns in diameter. It is nearly smooth to the touch, unlike a typical sintered-metal porous surface. Although there is a axial seam where the skin is welded after being formed around the suction body, that skin can be placed on the far side of the model for the experiments, so it should have no effect on the measurements, and it is more affordable to begin the research with flat welded skins of this type. Four more skins are being fabricated in 2018, using different hole patterns, but the same overall geometry, so they are interchangeable.

Possible geometries for the aft portion of the model were first investigated in Purdue University course project reports by Josh Edelman, Brandon Chynoweth, Katie Gray, and Greg McKiernan, by using the University of Minnesota STABL code, in Fall 2016. It became apparent that a substantial concave flare might be used, enabling study of the Görtler amplification of the streamwise vorticity introduced by the suction nonuniformities, although it was only possible to evaluate Görtler numbers, not Görtler N factors. The computational effort reported in this paper enabled a much more sophisticated design of the flared afterbody, to achieve the targeted range of Görtler N factor within the tunnel constraints.
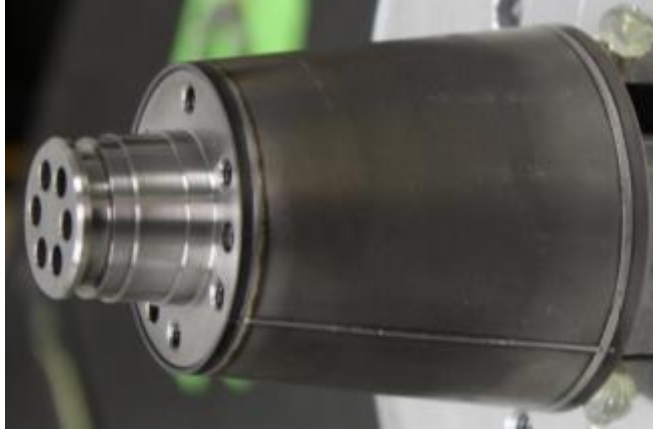
American Institute of Aeronautics and Astronautics

Figure 14.   Photograph of first suction section.

C. Detailed Description of Model and Instrumentation

The Suction Cone is a 7° half-angle sharp, circular cone that smoothly transitions into a flare with a radius of curvature of 1 m. The geometry is based Case 9 in Table 1, except that the total length of the cone is shortened so that the base diameter is 0.1016 m, to improve the probability that the model will start. The nose tip radius was measured to be 0.20 mm. There are four sensor ports around the azimuth on the flare, 0.4498 m from the nose tip. Three more sensor ports are spaced every 0.0254 m behind an azimuthal sensor port. Six PCB-132A high-frequency pressure sensors and one Schmidt-Boelter heat-transfer gauge were installed in the sensor ports. Four PCBs around the azimuth near the aft end of the cone section are used to finely adjust the angle of attack to 0.0 deg. by aligning the frequencies of the measured second-mode instability. Two additional PCBs were used to track second-mode instability growth along the flare. The Schmidt-Boelter heat transfer gauge is used to calibrate temperature-change measurements to heat transfer. The instrumented cone is shown in Figure 15. The sensors were electrically isolated and secured to the model with nail polish.
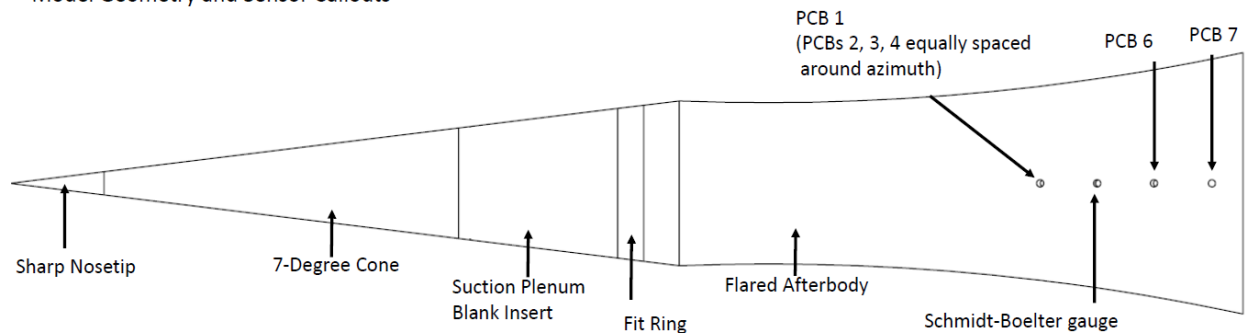

Figure 15.   Model geometry and sensor locations.

The internal static pressure of the model, both in the plenum and near the baseplate of the model, is measured in two locations with Kulite ETL-79-HA-DC-190-5A pressure sensors. The plenum pressure was measured using an 1/8 in. tube leading from the plenum to an ETL-79 sensor farther downstream inside the model. A sketch of this is shown in Figure 16. The pressure near the model base is measured by a second ETL-79 that screws directly into the baseplate of the model. The sensor wires leaving the model interior are sealed using Conax pressure fittings installed in the baseplate.
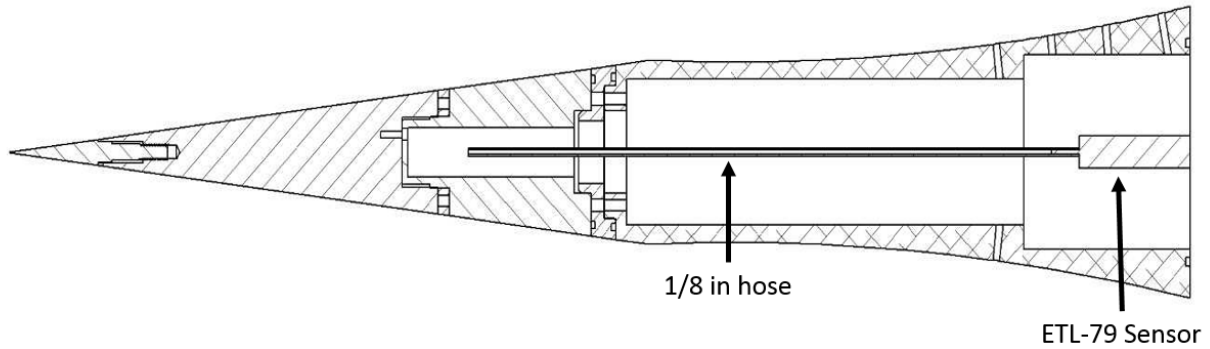
15

American Institute of Aeronautics and Astronautics

Figure 16. Cross section of the model depicting the 1/8 in. tube leading from the plenum to the ETL-79 pressure sensor in the model base.

Temperature-sensitive paint (TSP) is used to measure the temperature change on the surface of the model during a run. Before an entry in the tunnel, the flare of the model is primed with jet white spray paint and then TSP is applied via a paint gun. The TSP consists of the luminescent molecule Tris(2,22-bipyridine) dichlororuthenium(II) Hexahydrate (Ru(bpy)) dissolved in ethanol and mixed with Urethane Clearcoat and an activator. The molecule is excited during a run using two blue-light LEDs with a 465 nm wavelength. Pictures were taken with a Cooke Corporation PCO.1600 14-bit CCD camera. Before a run, pictures are taken with the room dark and with the blue LEDs on (called the Off images). During a run, the images are taken at 15 Hz. In post-processing, the ratio between the Run images and the Off images is used to calculate the surface temperature change. By comparing the Schmidt-Boelter gauge to a nearby patch of the surface temperature change during a run, a linear fit for converting temperature change to heat transfer is detemined (Ref. 43).

The detailed design of the model was carried out at Purdue, with the forecone and aft cone being fabricated in the AAE Department machine shop during Fall 2017. Fig. 17 shows a photograph of the model with a dummy solid section in place of the suction section.

Figure 17. Photograph of cone-flare model with dummy suction section

It was also necessary to develop a suction system to remove the boundary-layer air from above the model. At a tunnel stagnation pressure of 130 psia, the static pressure on the cone surface above the suction section is about 8 torr, according to a simple Taylor-Maccoll analysis. To achieve sonic flow through the suction skin, the internal pressure must be about 4 torr or less. Since the solenoid valve in the suction line is large enough that it must be placed outside the tunnel, a substantial volume of air at 130 psia must be exhausted from the suction plenum and suction lines in about 0.2 sec. in order to reach 4 torr. To enable reaching these very low pressures in this short time, the 500 cubic foot vacuum tank that was procured for the old Mach-4 Ludwieg tube was plumbed to the Mach-6 tunnel test area using a 6-inch aluminum line. It is not easy to measure such low pressures at the moderately high frequencies required, when the pressure sensor must survive the 130+ psia stagnation pressure before startup. However, a stopped Kulite ETL-79-HA0190-5A sensor was placed inside the suction model to make this measurement, after being carefully calibrated using two different vacuum sensors.

16

American Institute of Aeronautics and Astronautics

D. First Measurements of Static Pressure within the Suction Plenum

Finding the pressure inside the suction plenum during a run is not trivial. From a Taylor-Maccoll approximation, the ratio between the static pressure on the surface of a cone and the freestream stagnation pressure can be determined. For Mach 6 flow over a 7 deg. half-angle cone, this ratio is 1.244×10^{-3}. Consequently, with a freestream stagnation pressure of 30 psia (206843 Pa), near the maximum pressure where quiet flow was achieved at the time of these tests, the surface static pressure on the cone is 1.93 torr (257 Pa). In order to have "sonic suction," the maximum static pressure inside the plenum can be 54 percent of the cone surface static pressure. Ergo, in order to achieve sonic suction, the plenum static pressure must be less than 1.04 torr (138 Pa). Sonic suction is required to minimize data being transmitted from the suction surface into the freestream flow.

The static pressure inside the plenum is measured with a Kulite ETL-79-HA-DC-190-5A pressure transducer. The sensor is mechanically stopped near 5 psia (34474 Pa). An example of the static pressure measured in the plenum during runs with and without opening the suction system to vacuum ("Suction on" and "Suction off," respectively) is shown in Figure 18. For both runs, the freestream stagnation pressure was 29.1 psia (200637 Pa) with noisy flow. The mean of the static plenum pressure from 0.5 to 2.75 seconds with "suction on" was 2.56 torr (341 Pa), while for "suction off" it was 7.41 torr (988 Pa).

Due to limitations in the current suction plumbing, the highest freestream stagnation pressure tested with suction was 30 psia. Due to maintenance in the BAM6QT, the maximum quiet flow has recently been limited to around 27 psia. Other limitations in the suction plumbing resulted in leaks that allow the freestream static pressure to influence the static pressure inside the suction plenum. The measured plenum static pressure is not low enough for sonic suction to occur at this low stagnation pressure. Future tests will be made with a different vacuum plumbing system that leaks less, and at higher stagnation pressures, with quiet flow.
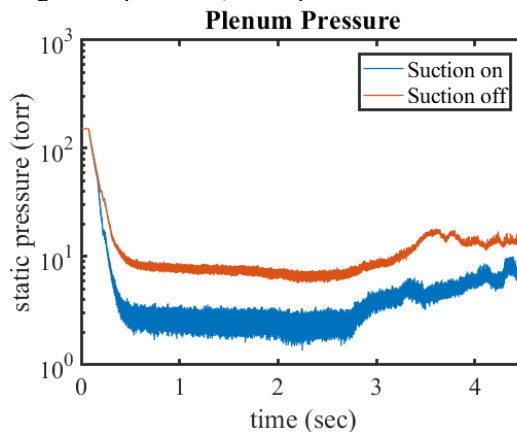

Figure 18. Time traces of static pressure inside suction plenum during runs with initial freestream stagnation pressure 29.1 psia.

E. First Measurements of the Effect of Suction on the Radiated Pressure Fluctuations

A pitot probe was used to measure the freestream pressure fluctuations radiated from the suction section. The probe used a Kulite XCQ-067-15A pressure sensor with a B screen. The probe was positioned an axial distance of 9.39 in. from the nose tip of the model. This corresponds to approximately the middle of the suction section. The probe assembly is motorized to allow radial traversing of the nozzle flow, in the vertical direction, perpendicular to the model centerline.

The power spectral densities of the freestream pressure fluctuations normalized by the freestream stagnation pressure were calculated from segments of data 0.01 seconds in length that occurred approximately 1 second into the run. Segments of 0.01 second corresponds to the duration the probe was programmed to dwell at that position before moving to traverse the flow. The probe was located 0.03 in. above the model. Figure 19 shows the power spectral densities for two runs with the suction system enabled and disabled (Suction on and Suction off, respectively) at comparable unit Reynolds numbers.

Enabling the suction system did not appear to have any effect on the flow near the model surface. This is not surprising, as the static pressure in the plenum was not low enough to allow sonic suction to occur during the run. Also, the freestream noise at this 30 psia noisy-flow condition may be dominating any pressure fluctuations in the

17

American Institute of Aeronautics and Astronautics

flow near the suction section. Clearly, these first measurements must be repeated at higher stagnation pressures, after the suction plumbing is improved, and after the tunnel returns to quiet flow at higher pressures.
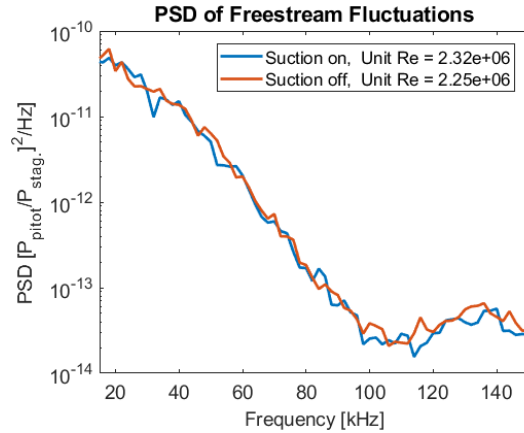

Figure 19. Power Spectra from Kulite pitot measurements 0.03 in. above the suction section at 9.39 in. from nose tip.

F. Pitot Traverses Above the Model with Suction System Enabled

In order to determine the effect of the suction system on the freestream flow above the model, pressure fluctuations were measured with the aforementioned pitot probe in the freestream flow near the model surface. The probe was initially positioned 0.03 in. above the surface of the model. During runs, the probe was traversed rapidly over a region of about 0.06 inches in 10 steps. It then returns to the initial position and repeats this 10 times over the course of a run. During the sets of steps, the Reynolds number is approximately constant. Figure 20 presents the sample power spectra of five such freestream fluctuations normalized by the freestream stagnation pressure measured during one set constant Reynolds number steps. For the example, the unit Reynolds number for the run is 2.32×10^6 per m with a freestream stagnation pressure of 30.1 psia. No distinguishable differences in fluctuations based on position were measured. Again, this is expected since even though the suction system was enabled, there was an insufficient pressure drop inside the plenum for sonic suction to occur through the porous skin. More measurements are needed with an improved suction-plumbing system, at higher stagnation pressures, after the tunnel returns to quiet flow at those higher stagnation pressures.
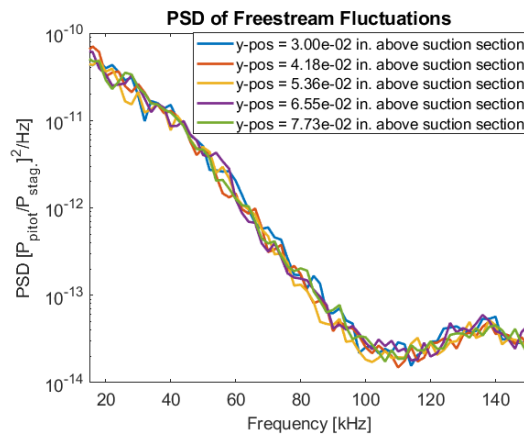

Figure 20. Freestream pressure fluctuations at 5 locations above the model surface. Unit Reynolds is 2.32×10^6 per meter. Stagnation pressure was 30.1 psia.

V. Summary and Concluding Remarks

Computations were performed for a total of 13 candidate axisymmetric cone configurations to identify a suitable model design for an experimental investigation of the effects of suction on Görtler instability in a Mach 6 flow. The

American Institute of Aeronautics and Astronautics

selected configuration meets the experimental constraints on forecone geometry and maximum cone diameter, while achieving a peak Görtler N-factor of approximately eight in the absence of any suction. DNS computations indicate that if Görtler-induced transition cannot be achieved via natural surface roughness on the wind tunnel model, then introducing an azimuthally periodic array of roughness elements with a peak height perturbation of 0.005 mm should certainly excite Görtler vortices that becomes strongly nonlinear within the cone length. The nonlinear vortex structures sustain secondary instabilities with an estimated N factor of 8, making the onset of transition over the cone model rather likely in this case. However, whether or not transition would actually occur via the nonlinear development of secondary instability modes will depend on the initial amplitude of those modes. The analysis presented herein also indicates that the most amplified modes of secondary instability originate from the Mack mode instability of the unperturbed boundary layer.

The design and fabrication of the wind-tunnel model and suction system are described. A few results from the first set of experiments are also reported. No useful conclusions can be drawn at this point, however. After the suction plumbing is improved, the four additional sections are procured, and the tunnel returns to quiet flow at higher pressures, it should be possible to assess the four risks described in Section IV.A. Future computational effort will targets the effects of suction on the generation and amplification of instability modes over the cone model. Preliminary results obtained thus far indicate that, because the Görtler instability is mainly driven by the concave surface curvature, suction has a relatively smaller influence on its amplification rates, in contrast to the strongly stabilizing influence of suction on other forms of stationary instability such as crossflow vortices.

Acknowledgments

References

[1] Schneider, S. P., "Development of Hypersonic Quiet Tunnels," *Journal of Spacecraft and Rockets*, Vol. 45, No. 4, July-August 2008, pp 641-664.

[2] Mack, L. M., Boundary-Layer Linear Stability Theory, in "Special Course on Stability and Transition of Laminar Flow," AGARD Report No. 709, pp. 3-1—3-81, 1984.

[3] Görtler, H., "On the Three-Dimensional Instability of Laminar Boundary Layers on Concave Walls," NACA TM 1375, 1954; translated from "Über eine Dreidimensionale Instabilität Laminarer Grenzschichten an Konkaven Wänden. Des. D. Wiss. Göttingen, Nachr 1940, 1940, 1 (2).

[4] Hall, P., "Taylor-Görtler Vortices in Fully Developed or Boundary-Layer Flows: Linear Theory," *J. Fluid Mech.*, Vol. 124, 1982, pp. 475–494.

[5] Hall, P., "The Linear Development of Görtler Vortices in Growing Boundary Layers," *J. Fluid Mech.*, Vol. 130, 1983, pp. 41–58

[6] Hall, P., "Görtler Vortices in Growing Boundary-Layers: The Leading-Edge Receptivity Problem, Linear Growth and the Nonlinear Breakdown Stage," *Mathematika*, Vol. 37(2), 1990, pp. 151–189.

[7] El-hady, N. M. and Verma A. K., "Growth of Görtler Vortices in Compressible Boundary Layers along Curved Surfaces," AIAA Paper 1981-1278, 1981.

[8] Hall, P. and Malik, M., "The Growth of Görtler Vortices in Compressible Boundary Layers," *J. Eng. Math.*, Vol. 23, 1989, pp. 239–251.

[9] Hall, P. and Fu, Y., "On the Görtler Vortex Instability Mechanism at Hypersonic Speeds," *Theoretical and Computational Fluid Dyn.*, Vol. 1(3), 1989, pp. 125–134.

[10] Fu, Y. and Hall, P., "Effects of Görtler Vortices, Wall Cooling and Gas Dissociation on the Rayleigh Instability in a Hypersonic Boundary Layer," *J. Fluid Mech.*, Vol. 247, 1993, pp. 503–525.

[11] Fu, Y., Hall, P., and Blackaby, N., "On the Görtler Instability in Hypersonic Flows: Sutherland Law Fluids and Real Gas Effects," *Phil. Trans. Royal Soc. A*, Volume 342, issue 1665, 1993, pp. 325–377

[12] Fu, Y. and Hall, P., "Crossflow Effects on the Growth Rate of Inviscid Görtler Vortices in a Hypersonic Boundary Layer," *J. Fluid Mech.*, Vol. 276, 1994, pp. 343–367.

[13] Dando, A. H. and Seddougui, S. O., "The Compressible Görtler Problem in Two-Dimensional Boundary Layers," *IMA J. Appl. Math.*, Vol. 51(1), 1993, pp. 27–67.

American Institute of Aeronautics and Astronautics

[14] Kobayashi, R. and Kohama, Y., "Taylor-Görtler Instability of Compressible Boundary Layers," *AIAA Journal*, Vol. 15, No. 12, December 1977.

[15] Whang, C. W. and Zhong, X. L., "Direct Numerical Simulation of Görtler Instability in Hypersonic Boundary Layers," AIAA Paper 1999-291, 1999.

[16] Whang, C. W. and Zhong, X. L., "Nonlinear Interaction of Görtler and Second Modes in Hypersonic Boundary Layers," AIAA Paper 2000-536, 2000.

[17] Whang, C. W. and Zhong, X. L., "Receptivity of Görtler Vortices in Hypersonic Bboundary Layers," AIAA Paper 2002-151, 2002.

[18] Whang, C. W. and Zhong, X. L., "Leading Edge Receptivity of Görtler Vortices in a Mach 15 Flow over a Blunt Wedge," AIAA Paper 2003-0790, 2003.

[19] Li, F., Choudhari, M. M., Chang, C.-L., Wu, M., and Greene, P. T., "Development and Breakdown of Görtler Vortices in High Speed Boundary Layers," AIAA Paper 2010-705, 2010.

[20] Ren, J. and Fu S., "Secondary Instabilities of Görtler Vortices in High-Speed Boundary Layers," *J. Fluid Mech.*, 781, 2015, pp. 388–421.

[21] vulcan-cfd.larc.nasa.gov (last accessed October 17, 2017)

[22] van Albada, G. D., van Leer, B. and Roberts, W. W., "A Comparative Study of Computational Methods in Cosmic Gas Dynamics," *Astronomy and Astrophysics*, Vol. 108, 1982, pp. 76–84.

[23] Edwards, J. R., "A Low-Diffusion Flux-Splitting Scheme for Navier-Stokes Calculations," *Computer and Fluids*, Vol. 6, 1997, pp. 635–659.

[24] Litton, D., Edwards, J., and White, J., "Algorithmic Enhancements to the VULCAN Navier-Stokes Solver," AIAA Paper 2003-3979, 2003.

[25] Cheatwood, F. M. and Gnoffo, P. A., "User's Manual for the Langley Aerothermodynamic Upwind Relaxation Algorithm (LAURA)," NASA TP 4674, April 1996.

[26] Li, F., Choudhari, M., Chang, C.-L., and White, J., "Analysis of Instabilities in Non-Axisymmetric Hypersonic Boundary Layers over Cones," AIAA Paper 2010-4643, 2010.

[27] Li, F., Choudhari, M., Paredes, P., and Duan, L., "High-Frequency Instabilities of Stationary Crossflow Vortices in a Hypersonic Boundary Layer," *Phys. Rev. Fluids*, Vol. 1, 2016, 053603.

[28] Wu, M. and Martin, M. P., "Direct Numerical Simulation of Supersonic Boundary Layer over a Compression Ramp," *AIAA Journal*, Vol. 45, No. 4, 2007, pp. 879–889.

[29] Jiang, G. S. and Shu, C. W., "Efficient Implementation of Weighted ENO Schemes," *J. Comp. Phys.*, Vol. 126, No. 1, 1996, pp. 202–228.

[30] Taylor, E. M., Wu, M., and Martin, M. P., "Optimization of Nonlinear Error Sources for Weighted Non-Oscillatory Methods in Direct Numerical Simulations of Compressible Turbulence," *J. Comp. Phys.*, Vol. 223, No. 1, 2006, pp. 384–397.

[31] Williamson, J., "Low-Storage Runge-Kutta Schemes," *J. Comp. Phys.*, Vol. 35, No. 1, 1980, pp. 48–56.

[32] Duan, L., Beekman, I., and Martin, M. P., "Direct Numerical Simulation of Hypersonic Turbulent Boundary Layers. Part 3: Effect of Mach Number," *J. Fluid. Mech.*, Vol. 672, 2011, pp. 245–267.

[33] Duan, L., Choudhari, M., and Li, F., "Direct Numerical Simulation of Crossflow-Induced Transition in a Swept Wing Boundary Layer," AIAA Paper 2013-2617, 2013.

[34] Beckwith, I. E. and Holley, B. B., "Görtler Vortices and Transition in Wall Boundary Layers of Two Mach 5 Nozzles," NASA TP-1869, 1981.

[35] Cosu, C., Chomaz, J. M., Huerre, P., and Costa, M., "Maximum Spatial Growth of Görtler Vortices," Flow, Turbulence, and Combustion, Vol. 65, 2000, pp. 369-392.

[36] Hall, P., and Horseman, N. J., "The linear Inviscid Secondary Instability of Longitudinal Vortex Structures in Boundary Layers," *J. Fluid Mech.*, Vol. 232, pp. 357-375, 1991.

[37] Li, F. and Malik, M. R. "Fundamental and Subharmonic Secondary Instabilities of Görtler Vortices," *J. Fluid Mech.*, Vol. 297, pp. 77-100, 1995.

[38] Li, F. and Choudhari, M., "Spatially Developing Secondary Instabilities and Attachment Line Instability in Supersonic Boundary Layers," AIAA Paper 2008-590, 2008.

[39] Li, F., Choudhari, M., Paredes, P., and Duan, L., "Secondary Instability of Stationary Crossflow Vortices in Mach 6 Boundary Layer over a Circular Cone," NASA/TM-2015-218997, Dec. 2015.

[40] Li, F., Choudhari, M., Paredes, P., and Duan, L., "High-Frequency Instabilities of Stationary Crossflow Vortices in a Hypersonic Boundary Layer," *Phys. Rev. Fluids*, Vol. 1, 2016, 053603.

[41] Moyes, A. J., Paredes, P., Kocian T. S., and Reed, H., "Secondary Instability Analysis of Crossflow on a Hypersonic Yawed Straight Circular Cylinder," AIAA paper 2016-0848, 2016.

[42] Paredes, P., Choudhari, M., and Li, F. "Instability Wave-Stream Interactions in a Hypersonic Boundary Layer at Glight Conditions," *J. Fluid Mech.* 2018 (In review).

[43] Sullivan, J. P., Schneider, S. P., Liu, T., Rubal, J., Ward, C., Dussling, J., Rice, C., Foley, R., Cai, Z., Wang, B., and Woodiga, S., "Quantitative G;obal Heat Transfer in a Mach-6 Quiet Tunnel," NASA-CR-2012-217331, Feb. 2012.

20